



Synthesis and characterization of magnetically separable Ag/AgCl–magnetic activated carbon composites for visible light induced photocatalytic detoxification and disinfection

Joanne Gamage McEvoy, Zisheng Zhang*

University of Ottawa, Department of Chemical and Biological Engineering, 161 Louis Pasteur Private, Ottawa, ON, Canada K1N 6N5



ARTICLE INFO

Article history:

Received 16 October 2013

Received in revised form 22 February 2014

Accepted 22 April 2014

Available online 2 May 2014

Keywords:

Ag/AgCl

Magnetic photocatalyst

Activated carbon

Adsorbent photocatalyst

ABSTRACT

A magnetic adsorptive photocatalyst composite Ag/AgCl–magnetic activated carbon (A-MAC) was proposed and investigated. Magnetic activated carbon was prepared by impregnation of AC with silica-coated magnetite particles synthesized via chemical co-precipitation and a modified Stöber process, and was then used to synthesize Ag/AgCl–MAC composites by a facile deposition-precipitation-photoreduction method. The prepared composites were characterized by X-ray diffraction, transmission and scanning electron microscopies, respectively, X-ray photoelectron spectroscopy, N₂ sorption, and ultraviolet-visible light diffuse reflectance spectroscopy. The magnetic properties of the composites were studied by superconducting quantum interference device magnetometry, and they were found to exhibit quasi-superparamagnetic behaviour. The visible light induced photoactivities of the samples were studied for the degradation of model organic pollutants, methyl orange and phenol, and cyclic degradation experiments were performed by recovering the composite by magnetic separation between runs. The prepared composites were also found to possess good activity for photocatalytic disinfection, inducing a 3-log reduction in *Escherichia coli* K-12 in 40 min under irradiation. The incorporation of silica-coated magnetite into AC was thought to influence morphology in the final photocatalyst-adsorbent composites, and the role of silica in preventing iron oxide dissolution in the photoreactive system was investigated and discussed.

© 2014 Elsevier B.V. All rights reserved.

1. Introduction

In recent years, efforts towards the development of solar photocatalysis have been made with the goal of improving process efficiencies in order to realize the scalability and practical utilization of this advanced oxidation process for the abatement of pollutants in a number of environmental effluents, such as for the treatment of recalcitrant dyes and polyhalogenated organics in industrial wastewaters. Of particular interest is the design and fabrication of highly efficient photocatalytic materials that can be excited by visible light abundant in solar radiation, which are engineered to possess low rates of recombination of the photo-excited electrons and holes [1]. These photocatalysts may overcome some of the difficulties inherent to use of the traditional photocatalytic TiO₂, such as its large band gap energy ($E_{bg} = 3.2$ eV).

One such material explored is the silver/silver halide composite photocatalyst [2], which possesses high efficiency for visible light utilization and low rates of electron-hole recombination due to the localized surface plasmon resonance exhibited by the incorporated silver nanoparticles. This phenomenon gives rise to unique optical properties arising from the collective oscillation of conduction electrons upon interaction with electromagnetic radiation, and can result in amplified absorption of visible light depending on the size and morphology of the nanoparticles. In the silver/silver halide system, nanosilver and silver halide act in concert to polarize the photoinduced charges, which facilitates electron-hole separation. Additionally, the silver halide can produce oxidizing species such as Cl⁰ or Br⁰ (for Ag/AgCl and Ag/AgBr, respectively), which enhance photodegradation [3].

Another approach to increasing photocatalyst efficiency involves the improvement of mass transfer characteristics by immobilization on or incorporation of porous media with the catalyst [4,5]. Synergistic increases in the activity of TiO₂-activated carbon composites have been reported, and are attributed to the presence of a common contact interface between the solids, where

* Corresponding author. Tel.: +1 613 562 5800x6110; fax: +1 613 562 5172.

E-mail addresses: jgamage@uottawa.ca (J. Gamage McEvoy), [\(Z. Zhang\)](mailto:zzhang@uottawa.ca).

the AC captures the pollutants by adsorption, allowing them to migrate continuously to the supported photocatalyst due to the presence of concentration gradients [6]. However, the need for incorporation of visible light active photocatalysts into these AC composites was emphasized in literature [7]. Additionally, the composites were reported to suffer from biofouling and the formation of biofilms, due to the biocompatibility of AC.

To address practical issues related to separation of suspended photocatalysts from slurry, the development of magnetically recoverable photocatalysts has become an active field of research. These photocatalysts may be two-component magnetic core@photocatalyst shell structures (such as $\text{Fe}_3\text{O}_4@\text{TiO}_2$ [8], $\gamma\text{-Fe}_2\text{O}_3@\text{TiO}_2$ [9]) or three component core@insulating interlayer@shell to prevent reaction between the photocatalyst and magnetic component itself (such as in $\text{Fe}_3\text{O}_4@\text{SiO}_2@\text{TiO}_2$ [10], and the surface plasmon resonance enhanced $\text{Fe}_3\text{O}_4@\text{SiO}_2@\text{AgCl:Ag}$ [11]). Ao et al. first proposed the hybridization of magnetic removal strategies with adsorbent photocatalyst composites by synthesizing TiO_2 -magnetic activated carbon composites, prepared by the impregnation of mixed-phase iron oxides into activated carbon, followed by sol-gel synthesis to deposit TiO_2 photocatalyst into the composite [12], and evaluated the photocatalytic activity for phenol degradation under ultraviolet (UV) light. Subsequent studies also investigated the photodegradation of an azo dye under visible and UV irradiation [13], and preparation of the composite using visible light active N-doped TiO_2 as the photocatalyst component [14]. In some cases, a photodissolution of the iron oxides was observed, since no SiO_2 passivation layer was used.

In our previous work, we proposed and developed $\text{Ag}/\text{AgCl-AC}$ composites to address the need for more efficient visible light utilization of adsorbent photocatalyst materials, and tested their photoactivity for the degradation of organic pollutants, methyl orange dye (MO) and phenol [15]. In these composites, nanosilver acted by surface plasmon resonance to induce enhanced visible light activity, while the silver and silver halide promoted charge separation, and AC concentrated the pollutant around the supported active sites. Due to the reported photocatalytic disinfection activity of silver/silver halide structures [16], and because of interest in impregnated nanosilver for the reduction of AC biocompatibility [17–19], the developed $\text{Ag}/\text{AgCl-AC}$ composites were also studied for the photocatalytic inactivation of *Escherichia coli* (*E. coli*) K-12 under visible light, and the antibacterial and photocatalytic disinfective capabilities of the catalyst were confirmed [20]. In the current study, we extend our previous work on the surface plasmon resonance enhanced $\text{Ag}/\text{AgCl-AC}$ composites towards magnetic removal strategies by the incorporation of magnetic activated carbon to synthesize $\text{Ag}/\text{AgCl-magnetic AC}$ composites ($\text{Ag}/\text{AgCl-MAC}$) and examine their activity for visible light induced degradation of organic and biological model pollutants.

2. Experimental

2.1. Materials

All materials were obtained from Fisher Scientific, unless otherwise mentioned, and were of reagent-grade or higher purity.

2.2. Synthesis of $\text{Ag}/\text{AgCl-magnetic activated carbon}$

2.2.1. Synthesis of silica-coated Fe_3O_4 nanoparticles

Magnetic Fe_3O_4 nanoparticles were synthesized by chemical co-precipitation of $\text{FeCl}_3 \cdot 6\text{H}_2\text{O}$ and $\text{FeSO}_4 \cdot 7\text{H}_2\text{O}$ at a molar ratio of 2.6:1. The iron salts were mixed in 100 mL of distilled deionized water at 70 °C under vigorous stirring [21,22]. A 2 M solution of NaOH was added dropwise until the pH was approximately 11. The

black solution formed was maintained at 70 °C under magnetic stirring for 1 h to ensure growth of the nanoparticles, and the mixture was then cooled to room temperature (~25 °C) in ambient air. The precipitate was collected by magnetic separation, and was rinsed with distilled deionized water multiple times to obtain a neutral pH in the product. The black Fe_3O_4 particles were then rinsed three times with absolute ethanol, filtered, dried overnight, and ground in an agate mortar for 2 min.

Silica coating of the obtained Fe_3O_4 nanoparticles was performed using a modified Stöber process [11,23]. A dispersion of 1 g Fe_3O_4 nanoparticles in 20 mL of 0.1 M sodium dodecyl sulphate was prepared by sonication for 10 min. The mixture was vigorously stirred for 30 min, followed by the successive addition of 20 mL of absolute ethanol, 6 mL of concentrated ammonia, and 5 mL of tetraethyl orthosilicate. The reaction was maintained at 50 °C for 3 h, and the grey silica-coated Fe_3O_4 nanoparticles obtained were separated magnetically, rinsed with distilled deionized water and absolute ethanol three times, and dried at room temperature overnight.

2.2.2. Synthesis of magnetic activated carbon (MAC)

Magnetic activated carbon was prepared by impregnation of unmodified commercial Darco G60 activated carbon (100 mesh, Sigma-Aldrich) with the silica-coated magnetic iron oxide nanoparticles. Activated carbon was added in a certain amount to a solution of 0.6 g of coated nanoparticles in 200 mL water, which had previously been dispersed by sonication for 10 min. The activated carbon-nanoparticle mixture was then stirred for 1 h, and the solid phase was collected by a magnet and dried at 40 °C. The silica-coated nanoparticles and AC were mixed at various weight ratios, as described in Table 1.

2.2.3. Synthesis of $\text{Ag}/\text{AgCl-MAC}$

$\text{Ag}/\text{AgCl-MAC}$ composites were prepared using an impregnation-precipitation-photoreduction method, as previously reported for the synthesis of $\text{Ag}/\text{AgCl-AC}$ [15]. The weight ratio of Ag/AgCl to activated carbon was maintained at 2.5:1 in all of the composites, calculated as if all of the AgCl was reduced to Ag . The weight ratios and equivalent weight fractions of the components in the prepared $\text{Ag}/\text{AgCl-MAC}$ composites are shown in Table 1, where $\text{Ag}/\text{AgCl-MAC}$ is denoted by A-MAC, and $\text{Ag}/\text{AgCl-AC}$ is denoted A-AC.

2.3. Characterization

X-ray diffraction (XRD) patterns were collected using a Rigaku Ultima IV XRD apparatus with a $\text{CuK}(\alpha)$ source ($\lambda = 0.15418 \text{ nm}$) operating at 40 kV and 44 mA. Transmission electron microscopy imaging was performed using an FEI (formerly Phillips) Tecnai F20 G2 field emission transmission electron microscope (TEM) equipped with an energy dispersive X-ray (EDS) detector for spectrometry. Histograms of particle size distributions were constructed using particle size measurements made on digital TEM images with Canon MeasureIT software. The morphology of the samples was investigated using a Tescan VegaII XMU field emission scanning electron microscope (SEM), with Au/Pd alloy coated samples (coated with an Anatech Hummer VII sputter coater). SEM-EDS was also performed using an energy dispersive X-ray detector. X-ray photoelectron spectroscopy (XPS) was studied on a Kratos Analytical Axis Ultra DLD instrument, using monochromated Al X-rays at 140 W. The surface areas, total pore volumes, and micro-porosity data were obtained from N_2 sorption isotherms at 77 K, using automatic adsorption apparatus and measurement systems (ASAP 2020, Micromeritics and Nova 4200E, Quantachrome). The Brunauer, Emmett, and Teller (BET) surface areas of the samples were calculated using a multi-point estimation, the total

Table 1

Composition of photocatalysts prepared at various weight ratios.

Catalyst	Weight ratios		Equivalent weight fractions		
	SiO ₂ –iron oxide: AC	SiO ₂ –iron oxide: AC: Ag/AgCl	SiO ₂ –iron oxide	AC	Ag/AgCl
1:3 A-MAC	1:3	0.33:1:2.5	0.0862	0.261	0.653
1:5 A-MAC	1:5	0.2:1:2.5	0.0541	0.270	0.676
1:7 A-MAC	1:7	0.14:1:2.5	0.0385	0.275	0.687
A-AC	–	0:1:2.5	0	0.286	0.714

pore volumes were calculated using the volumes of adsorbed N₂ at $P/P_0 = 0.977$, and the t -plot method was used to calculate micropore volumes and external surface areas. The Barrett–Joyner–Halenda method was used for the adsorption branch to calculate the pore size data. Ultraviolet-visible (UV–vis) diffuse reflectance spectra were measured on a Thermo Evolution 300 spectrophotometer (ThermoScientific) equipped with a Praying Mantis diffuse reflectance accessory over the range of 230–900 nm. Isothermal magnetization data was collected in the field range from -4×10^4 to 4×10^4 Oe at 300 K using a Quantum Design magnetic properties measurement system (MPMS) superconducting quantum interference device (SQUID).

2.4. Photocatalytic degradation

2.4.1. Photoreactor

To quantify photocatalytic degradation, a slurry reactor was used in a constructed reflective housing to prevent outside light from entering the system. Illumination was provided by a 300 W ELH tungsten halogen bulb (Ushio) with a UV filter (Kenko Zeta, $\lambda > 410$ nm, transmittance > 90%) at a distance of 10 cm from the beaker. The irradiation was measured using a quantum meter (Biospherical QSL-2100; 400 nm < λ < 700 nm), and was found to be approximately 4.7×10^{-3} Einstein m⁻² s⁻¹. Cooling was provided by an external cooling jacket, and the temperature of the reaction was controlled to $20^\circ\text{C} \pm 2$.

2.4.2. Photodegradation of methyl orange (MO)

For the photocatalysis tests, 200 mL of MO solution was allowed to equilibrate in the dark with 0.5 g L⁻¹ of catalyst under constant magnetic stirring at 180 rpm for 2 h prior to each experiment. Photocatalytic degradation was then performed for 2.5 h in the presence of visible light irradiation. For all tests, samples were drawn periodically, centrifuged, and the supernatant was analyzed at a single wavelength using a spectrophotometer (Genesys 10UV, ThermoScientific). The peak absorbance used for MO was $\lambda = 463$ nm. The initial MO concentration was 25 mg L⁻¹. The MO removal from solution was expressed relative to the catalyst dosage, and was given by q_t (mg MO g⁻¹ catalyst), calculated according to the following formula:

$$q_t = V \frac{(C_i - C_t)}{W} \quad (1)$$

where the initial MO concentration in the aqueous phase, and that at time t (min) are denoted by C_i and C_t , respectively (mg L⁻¹), V is the volume of MO solution (L), and W is the mass of composite used (g). The broad-scan UV–vis data for MO adsorption and degradation was collected on a Biochrom Ultrospec 60 UV–vis spectrophotometer. To evaluate the magnetic recovery and recyclability of the composite, cyclic adsorption–photocatalysis runs were performed by recovering the catalyst magnetically between cycles and redispersing it into fresh MO solution before each re-use. Photolysis was measured by MO degradation in the absence of catalyst, and the error associated to the experiments was estimated as the standard deviation between triplicate runs.

2.4.3. Photodegradation of phenol

Adsorption and photodegradation of phenol was also studied in the photosystem using the same methodology and parameters described for MO experiments, but the initial concentration used was 13 mg L⁻¹, and the supernatant was analyzed spectrophotometrically at a peak absorbance of $\lambda = 270$ nm. The photocatalytic degradation of phenol was carried out for 3 h after the initial dark adsorption period.

2.4.4. Iron oxide photodissolution

Iron oxide photodissolution was investigated by monitoring Fe⁺ concentration in solution using inductively coupled plasma mass spectrometry (ICP-MS) on an Agilent HP 4500. A 5 g L⁻¹ slurry of A-MAC catalyst in 50 mL distilled deionized water was magnetically stirred under irradiation at 180 rpm for 2.5 h, and samples were withdrawn periodically. The catalyst was then separated by centrifugation at 14 800 rpm for 5 min, and the supernatant was removed and stabilized with 5 vol% nitric acid prior to analysis. The trials were performed for the 1:7 A-MAC composite, and for a reference 1:7 A-MAC material prepared using iron oxide nanoparticles with no silica coating.

2.4.5. Silver ion elution

The elution of silver ions (Ag⁺) from the prepared A-MAC composite was also measured using ICP-MS. 5 g L⁻¹ of catalyst (1:5 A-MAC) in 50 mL distilled deionized water was magnetically stirred at 160 rpm in the dark for 1 h, and 1 mL samples were withdrawn periodically. The samples were centrifuged and the supernatant was removed and acidified before analysis. For all ICP measurements, the analyses were performed for triplicate samples.

2.5. Photocatalytic disinfection

2.5.1. Bacterial strain

Wild-type *E. coli* K-12 (TG1 strain) was used for all bacterial inactivation studies, due to its non-pathogenicity and its use as a common model in laboratory experiments. It was obtained from Dr. Christopher Q. Lan in the Department of Chemical and Biological Engineering at the University of Ottawa, and was maintained as a laboratory strain.

2.5.2. Cell culture and enumeration

All inactivation trials were performed in triplicate, and all materials were sterilized for 20 min at 121 °C prior to use. The inactivation was quantified as loss of culturability of the bacteria in the disinfection studies. Bacterial cultures were prepared by growing *E. coli* K-12 (TG1) aerobically in Luria–Bertani medium (Difco LB broth, Miller; containing 10 g L⁻¹ tryptone, 5 g L⁻¹ yeast extract, and 10 g L⁻¹ NaCl) on a rotary shaker at 37 °C until the stationary phase was reached. The initial concentration from the overnight culture was determined by serial dilution and plating using a plated volume of 25 µL. Aliquots were spread on solid LB agar plates in triplicate for each dilution, and incubated at 37 °C for 18 h. Bacterial enumeration was performed using standard plate counts for viable and cultivable bacteria, and counts obtained were used to calculate the cell concentration in colony forming units (CFU) mL⁻¹.

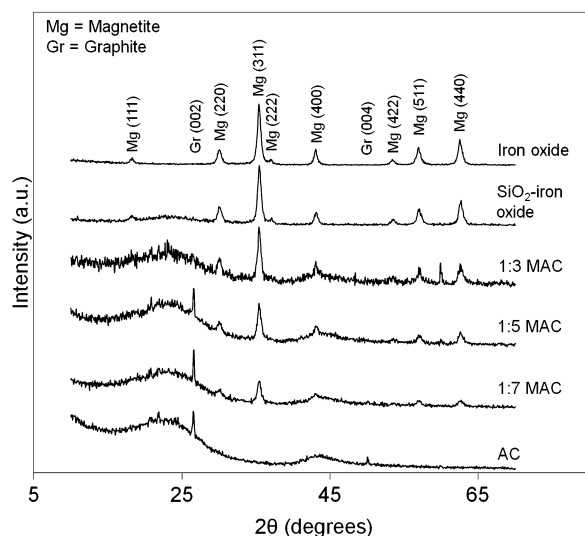


Fig. 1. XRD patterns for iron oxide, SiO₂–iron oxide, AC, and magnetic AC prepared at various ratios.

2.5.3. Temporal course of inactivation

The temporal course of inactivation was studied using 50 mL of saline (0.9 wt% NaCl) spiked with bacteria in a 100 mL Pyrex beaker. The initial bacterial suspension was prepared by centrifuging 1 mL of bacterial culture at 14 800 rpm for 5 min and resuspending the pellet in saline. This centrifugation and washing procedure was repeated three times to remove the growth media. The bacterial suspension was then used to prepare the spiked solution, controlling the initial concentration to approximately 10⁶ CFU mL⁻¹. Catalyst was then added to the bacterial suspension at a loading of 5 g L⁻¹, and the mixture was magnetically stirred at 160 rpm under visible light irradiation (provided by a filtered 300 W Ushio ELH lamp). During the disinfection, the temperature was maintained constant at 20 °C ± 2 using a water bath, and samples were collected periodically. The samples were serially diluted in saline and spread onto LB agar plates using aliquot volumes ranging from 25 to 200 µL. The plates were then incubated and bacteria enumerated using the standard plate count method. Control runs were performed in the absence of photocatalyst and light, respectively.

3. Results and discussion

3.1. Catalyst characterization

3.1.1. X-ray diffraction

The phase structure and crystallinity of the prepared materials were investigated by XRD, and the results are given in Fig. 1 for the prepared iron oxide and magnetic activated carbons, respectively. The diffraction pattern obtained for the pure iron oxide was well-indexed to the cubic spinel structure of magnetite, and characteristic peaks at 18.3°, 30.1°, 35.4°, 37.1°, 43.1°, 53.4°, 56.9°, 62.5° were observed, corresponding to the (111), (220), (311), (440), (422), (511), and (440) faces respectively, in good agreement with JCPDS card #19-0629.

Upon introduction of the silica coating, the patterns observed contained the same characteristic magnetite peaks, as well as a small broad amorphous halo due to SiO₂ between 20° and 30°. The unmodified AC also exhibited mainly amorphous structure, with the exception of hexagonal (002) and (004) graphitic peaks, which indicated that small regions of crystallinity were present [24]. The XRD patterns for all prepared magnetic AC materials exhibited the characteristic peaks observed for the magnetite phase, as

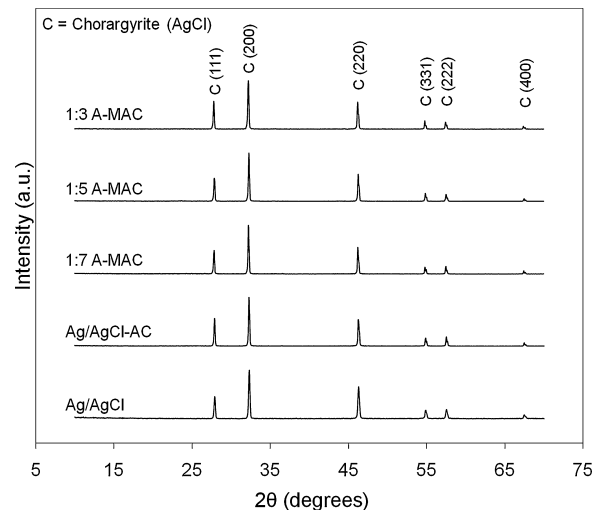


Fig. 2. XRD patterns for Ag/AgCl, Ag/AgCl–AC, and Ag/AgCl–magnetic AC photocatalysts prepared at various ratios.

well as the (002) graphite plane, except for the MAC prepared with a magnetic particle loading of 1:3. In the 1:3 MAC pattern, the graphitic peak was not noticeable due to the relatively lower activated carbon content in the magnetic material, in accordance with the compositions given in Table 1. The appearance of a peak at ~60° also suggested the transformation of some magnetite into an impurity phase, such as the less magnetic maghemite, or nonmagnetic goethitic iron oxide in accordance with JCDPS card #29-0713. The formation of this impurity phase may have been caused by the overloading of activated carbon with magnetite nanoparticles and their subsequent transformations, especially upon prolonged exposure to the oxidative environment used during the drying step in the MAC synthesis. The formation of the less-magnetic maghemite phase from oxidation of magnetite has been found to be dependent on a number of experimental and environmental conditions, such as the particle sizes of magnetite, water content, and temperature [25,26]. Nonmagnetic goethite may have been formed from this maghemite oxidation product, and the direct formation of goethite from magnetite may have also occurred in this system [27]. These transformations were not as pronounced for the materials prepared using lower iron oxide: AC ratios.

The XRD patterns of composite A-MAC photocatalysts were also investigated, and the results are given in Fig. 2, with pure Ag/AgCl and the nonmagnetic Ag/AgCl–AC shown for reference. All of the patterns observed exhibited peaks at 27.8°, 32.2°, 46.2°, 54.8°, 57.5°, and 67.5° corresponding to the (110), (200), (220), (331), (222), and (400) reflections of chlorargyrite (JCDPS card #31-1238). The major diffraction peaks for the (111) and (200) planes of silver, at 38.1° and 44.3°, respectively, were not easily observable in the AC composites, and this was thought to be due to the low content, small particle size, and high dispersion of the photo-reduced silver on the surface of AgCl–AC and on Ag/AgCl–MAC [28].

3.1.2. TEM/SEM observation

Typical bright-field TEM images for the prepared iron oxide, SiO₂–coated iron oxide, and a representative magnetic activated carbon (1:5 MAC) are given in Fig. 3. From Fig. 3a and b, the iron oxide nanoparticles prepared possessed regular spherical shapes, and had an average diameter of 10.5 ± 2.3 nm. The coating procedure yielded SiO₂–coated iron oxides, as seen in Figs 3c and 2d, where the dark, electron-dense spheres observed were attributable to iron oxide, while the light regions surrounding them were the outer silica layers formed on the magnetic nanoparticles. This implied that a core-shell structure was created through the

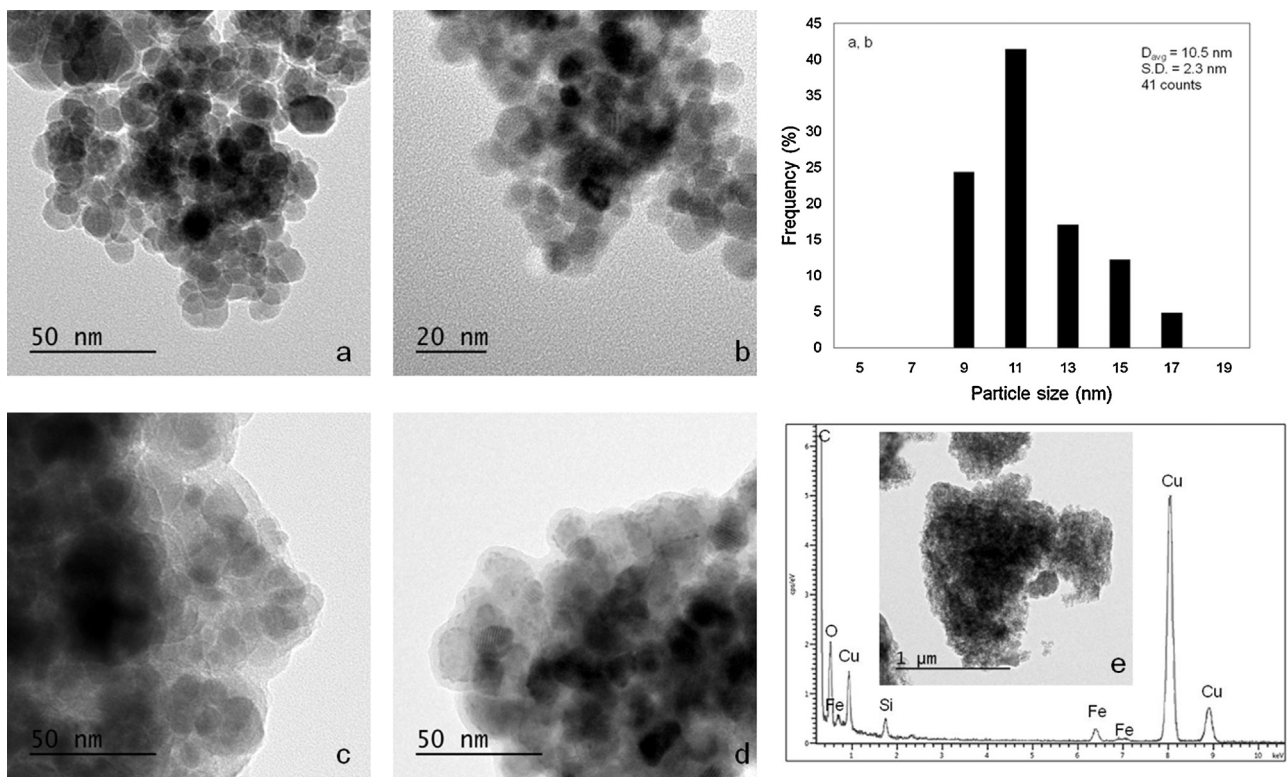


Fig. 3. TEM images of (a) and (b) iron oxide NPs; (c) and (d) SiO₂-iron oxide; (e) 1:5 A-MAC. The histogram for iron oxide NPs and EDS data for (e) are also shown.

modified Stöber process, with a silica thickness ~5 nm. The size of the individual core-shell particles observed was ~21–30 nm.

From the TEM image of 1:5 MAC given in Fig. 3e, the silica-coated iron oxide nanoparticles were thought to be well adhered to or incorporated within the larger activated carbon structure. The TEM-EDS pattern shown for the MAC confirmed the presence of carbon, iron, silicon, and oxygen in the μm-scale structures shown in Fig. 3e, where the presence of copper in the spectrum was due to the copper grid used for observation. Additional TEM imaging was performed on a representative A-MAC (1:5), and is given in Fig. S1. Upon deposition of the photocatalyst into 1:5 MAC, dark, electron-dense regions were observed on the adsorbent, and shadowed other structures present in the composite. This shadowing effect was thought to be due to the high coverage, high electron density, and three-dimensional nature of Ag/AgCl photocatalyst on the surface of MAC, and prevented direct observation of the interfaces between the adsorbent host structure, Ag/AgCl, and magnetic nanoparticles. However, in some cases, dark photocatalyst clusters could be observed, as seen in Fig S1b.

SEM imaging was also performed to study the structure and morphology of the prepared composites, and the results are shown in Fig. 4 for a representative Ag/AgCl-magnetic AC (1:5 A-MAC), with the morphology of nonmagnetic A-AC shown for reference. The Ag/AgCl was observed to tightly adhere to the surfaces of the magnetic activated carbon to form a dense photocatalyst network, which was not the case for the nonmagnetic AC composite. This was thought to be due to influence of silica-coated iron oxides incorporated into the AC on the deposition behaviour of AgCl. The silica coating may have affected electrostatic interactions between silver nitrate and activated carbon used in the synthesis by making the magnetic AC composite more negatively charged overall in the aqueous-based impregnation than the pure AC. Silver nitrate was also expected to have a high affinity for SiO₂ in the aqueous synthesis solution [22], so silica-coated iron oxides on the surface of AC may have acted as preferential host sites for silver

ion deposition. The photoreduced metallic silver could be easily observed on the surface of the AgCl particles in the composite (as shown inset), and was found to range from 115 to 180 nm on the surface of larger AgCl particles measuring from 1.2 to 1.7 μm.

In addition, comparison of the structures of synthesized MAC and A-MAC are given in Fig. S2a and b, respectively, for the 1:5 composite. The pure MAC was composed of textured micron-scale carbonaceous structures, similar to the TEM image shown in Fig. 3e. Upon incorporation of the photocatalyst, superstructures formed from deposition of Ag/AgCl onto the surface of the MAC host material, as seen in Fig. S2b. SEM-EDS spectra from 1:5 A-MAC were also collected, and the results are shown in Fig. S3, where both photocatalyst-dominated structures and carbon-dominated regions were observed in the heterogeneous composite. It should be noted that Pd and Au were present in these spectra due to the sputter coating used for imaging.

3.1.3. X-ray photoelectron spectroscopy

The XPS full-scan spectra for a representative magnetic activated carbon (1:5 MAC) and its corresponding Ag/AgCl composite (1:5 A-MAC) are shown in Fig. 5a and b, respectively. In both spectra, peaks assigned to the Fe 2p states at ~714.5 were very weak or unobservable relative to the strong Si 2s and 2p states present, indicating that the coating procedure resulted in complete coverage of the iron oxide spheres by the SiO₂ layer [29]. Additionally, the presence of the silicon peaks in both surface XPS spectra indicated that some of the SiO₂-iron oxide structures incorporated into AC occupied its outer surface, and remained exposed even after AgCl deposition.

3.1.4. N₂ sorption-desorption isotherms

The structure and porosity characteristics of the samples were studied, and nitrogen sorption isotherms obtained are shown in Fig. 6a for AC and a representative magnetic AC (1:5 A-MAC), and in Fig. 6b for various prepared Ag/AgCl-magnetic AC composites (1:5

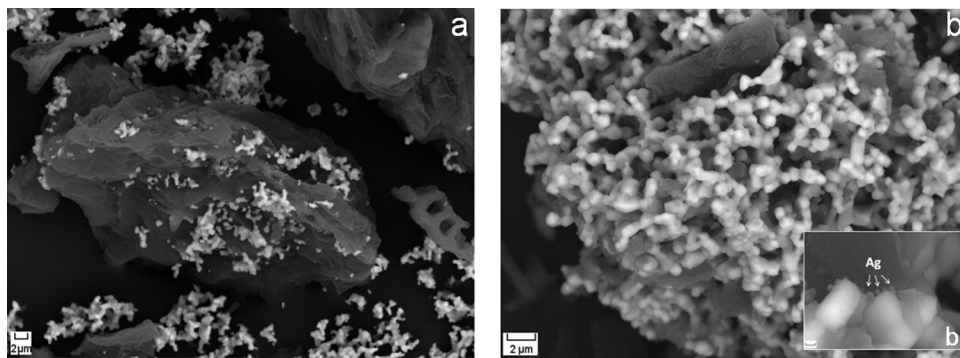


Fig. 4. SEM images of (a) A-AC, and (b) 1:5 A-MAC; (scale bar in inset is 200 nm).

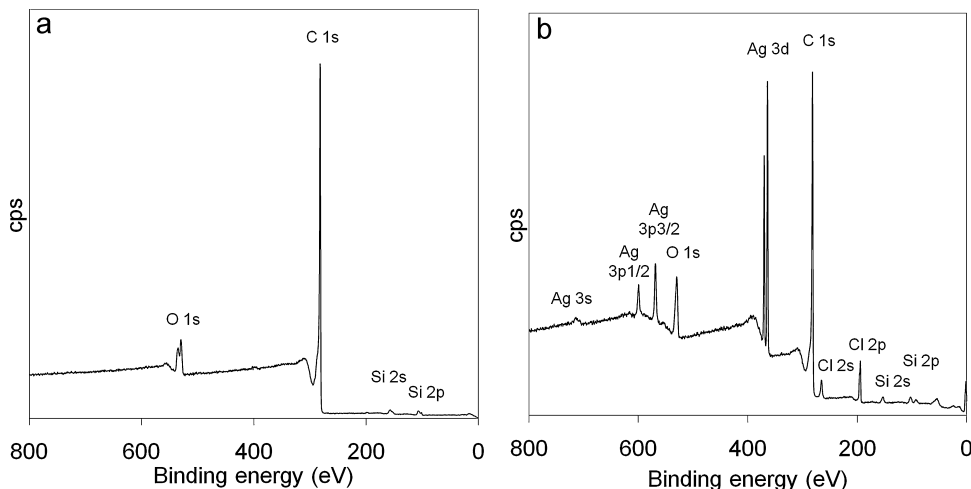


Fig. 5. XPS spectra for (a) 1:5 MAC, and (b) 1:5 A-MAC.

and 1:7 A-MAC, respectively), with the nonmagnetic A-AC shown for reference. All of the isotherms observed were classified as Type IV by IUPAC standards [30], with H4 hysteresis in the desorption branch due to the presence of mesopores [31].

From the isotherms obtained, parameters related to structural and textural characteristics of the synthesized materials were calculated, and are summarized in Table 2. Consistent with the results observed for the nonmagnetic A-AC composite with respect to the nonmagnetic AC host material, the BET surface area, total pore volume, as well as the micro- and mesopore volumes all decreased upon introduction of Ag/AgCl into the magnetic 1:5 MAC material.

Interestingly, although the total pore volume and microporosity of pure AC decreased after iron oxide addition, the external surface area increased. This was thought to be due to the creation of mesopores and macropores by silica-coated iron oxide aggregates on the surface of the AC structure, as reflected in the increase in pore diameter. Additionally, deposition of magnetic nanoparticles into the larger mesopores may have also caused pore-blocking of the micropore channels, since mesopores were the main throughfares to the microporous regions [32]. Based on SEM observations of the particle sizes of Ag/AgCl formed, they were not thought to enter the pore structure of the MAC host material, but instead formed

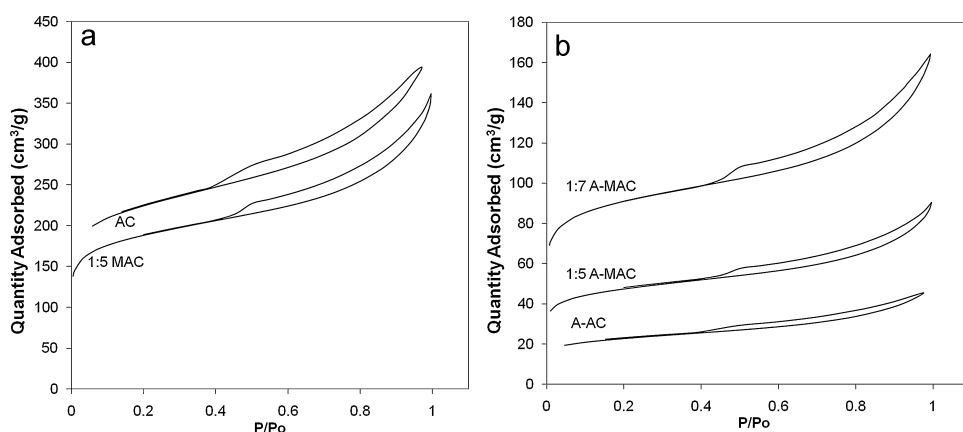


Fig. 6. N₂ sorption isotherms for (a) AC and 1:5 MAC; and (b) 1:7 A-MAC, 1:5 A-MAC, and A-AC, respectively.

Table 2

Structural and textural characteristics for A-MAC materials calculated from N₂ sorption isotherms.

Catalyst	Property					
	BET surface area (m ² g ⁻¹)	Total pore volume (cm ³ g ⁻¹)	Micropore volume (cm ³ g ⁻¹)	Micropore surface area (cm ² g ⁻¹)	External surface area (cm ² g ⁻¹)	Average pore diameter, BJH ads. (nm)
AC	811	0.609	0.269	510	201	3.624
A-AC	77.1	0.070	0.025	48.0	26.1	3.621
1:5 MAC	645	0.237	0.159	341	304	6.36
1:5 A-MAC	162	0.128	0.041	89.5	72.9	6.59
1:7 A-MAC	344	0.237	0.085	184	127	6.57

"egg-shell" composites, where the photocatalyst mainly deposited in clusters on the outside surface of AC [32], causing the observed decreases in surface area and porosity between the 1:5 MAC and A-MAC, respectively. The 1:7 A-MAC composite had a higher BET surface area than 1:5 A-MAC, since the host 1:7 MAC had less magnetic particles incorporated into it and occupying its pore volume and external surface than in the 1:5 MAC. The volume contribution of micropores to the total pore volume was similar for A-AC and both A-MAC samples studied, and ranged from 32 to 36%.

3.1.5. UV-vis diffuse reflectance spectroscopy

The UV-vis absorption spectra for the prepared Ag/AgCl-magnetic activated carbon composites were studied, and are given in Fig. 7 for a representative sample (1:5 A-MAC), as well as for Ag/AgCl-AC, pure Ag/AgCl, and unreduced AgCl. All of the samples were observed to have an absorbance edge at ~385 nm, corresponding to the band gap of AgCl ($E_{\text{bg, indirect}} = 3.25 \text{ eV}$ [33]). Additionally, the photoreduced samples exhibited broad absorption from 400 to 900 nm attributable to surface plasmon resonance of metallic silver nanoparticles produced during irradiation. This broad absorption band was not observed for the unreduced AgCl, evidencing the role and efficacy of photoreduction. The broadness of the absorption band observed in the partially reduced samples was thought to be due to the presence of multiple plasmonic oscillation frequencies, which were caused by a variation in the shapes and diameters of Ag nanoparticle clusters formed [2].

3.1.6. SQUID magnetometry and magnetic separation

The magnetic properties of the synthesized materials were probed by SQUID magnetometry, and the room temperature magnetic hysteresis loop for the synthesized iron oxide is shown in Fig. 8. Hysteresis loops for 1:5 magnetic AC, and 1:5 Ag/AgCl-magnetic AC composites are given in Fig. S4. The associated magnetic parameters of saturation magnetization (Ms),

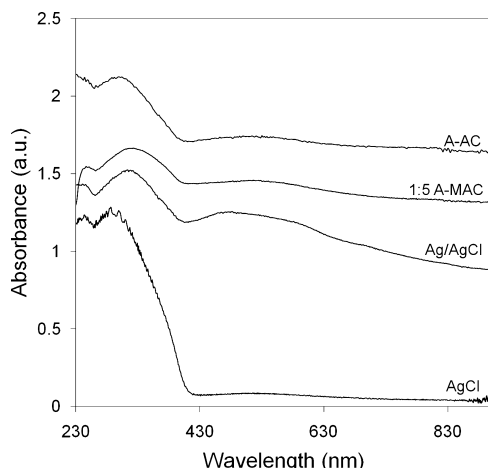


Fig. 7. UV-vis absorption spectra for a representative Ag/AgCl-magnetic AC (1:5 A-MAC), A-AC, Ag/AgCl, and unreduced AgCl, respectively.

coercive field (Hc), and remanent magnetization (Mr) are summarized in Table 3.

The prepared iron oxide nanoparticles exhibited quasi-superparamagnetic behaviour, as evidenced by their low coercive field and remanent magnetization. The prepared magnetic activated carbons (1:5, 1:7) and Ag/AgCl-magnetic AC composite (1:5 A-MAC) also showed similar behaviour, with Hc ranging from 35 to 45 Oe, and Mr from -0.03 to 0.17. The saturation magnetization of magnetic activated carbon increased with increasing iron oxide content, although this value decreased upon introduction of the Ag/AgCl component, due to the large relative weight contribution by the nonmagnetic photocatalyst. However, for all materials prepared, the squareness ratios (Mr/Ms) observed were less than 5.2%, confirming their quasi-superparamagnetic behaviour at room temperature [34,35]. The acceptable saturation magnetization values indicated that the prepared materials were suited to magnetic removal strategies, as shown in Fig. S5 for the 1:5 A-MAC exposed to two 12.5 mm cubic NdFeB cube magnets, each having surface field strengths of 5.75×10^3 Gauss, for 5 min. The low coercivity and remanent magnetization observed also implied that catalyst aggregation could be prevented and that the catalyst could be easily redispersed for recovery or reuse in a suspension [36].

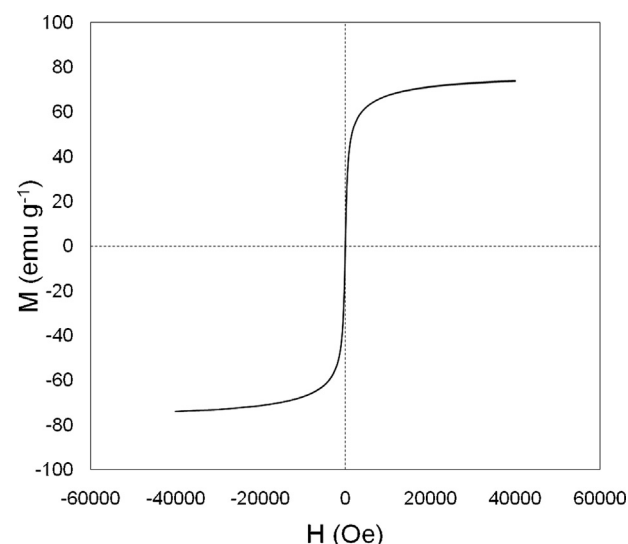


Fig. 8. Room temperature magnetization hysteresis loop for synthesized iron oxide nanoparticles.

Table 3

Room temperature magnetic properties of iron oxide nanoparticles and representative magnetic composites: 1:7 MAC, 1:5 MAC, and 1:5 A-MAC, respectively.

Sample	Ms (emu g ⁻¹)	Hc (Oe)	Mr (emu g ⁻¹)
Iron oxide NPs	74.02	26	2.42
1:5 MAC	4.05	45	0.021
1:7 MAC	3.36	45	0.17
1:5 A-MAC	0.61	35	-0.030

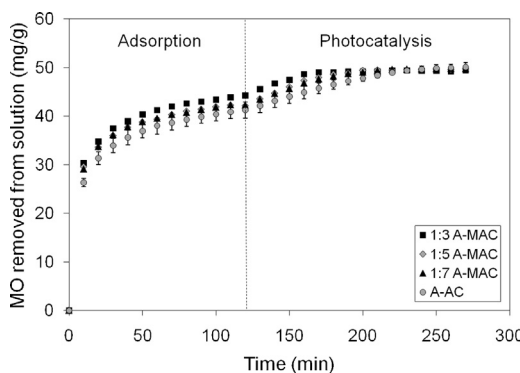


Fig. 9. Adsorption and subsequent photocatalysis using A-MAC prepared at various weight ratios—representative error bars shown.

3.2. Photocatalytic degradation of organic compounds

3.2.1. MO adsorption and photodegradation

Adsorption and photodegradation were studied for a model organic compound, MO dye, which was found to have a negligible photolysis over 2.5 h under visible light irradiation. The prolonged adsorption-photocatalysis trials consisted of a 2 h dark adsorption period, followed by illumination for 2.5 h, and the results obtained are shown in Fig. 9 as MO removed from solution per weight of catalyst used for the prepared materials, with the non-magnetic Ag/AgCl-AC composite data shown for reference. The magnetic composites exhibited similar adsorption-photocatalysis behaviour as nonmagnetic Ag/AgCl-AC, where MO adsorption pseudo-equilibrium was achieved after 2 h, and a sharp change in MO removal occurred upon irradiation and continued until the pollutant was almost fully removed from solution. This increase in removal upon irradiation was thought to be due to photoexcitation of the catalyst and subsequent photocatalytic action of radicals and reactive species on the dye, initiating a dynamic adsorption-photocatalytic degradation process.

The removal of MO by adsorption from solution was qualitatively similar or within error for the AC and MAC composites, ranging from 41.2 to 44.2 mg MO g⁻¹ composite after 2 h, and this dark adsorption was thought to be governed by a number of factors. The methyl orange dye adsorbate was considered to be a bulky molecule, with a molecular size of 1.31 × 0.55 × 0.18 nm [37], and it was previously indicated that pores having diameter between 2.5 and 4.5 nm were most suitable to MO adsorption [6], since pores with width or diameter 1.7–3 times larger than the adsorbates provided favourable adsorption [38]. Based on this, it followed that although the BET surface area observed for pure A-AC was much lower than that for the prepared A-MAC materials, adsorbate removal was also likely influenced by preferential adsorption of MO into the smaller pores present/accessible in A-AC. Based on the size of MO, it was also implied that much of MO adsorption took place in the external surface area (mesopores, macropores) of the composite catalysts, and that increasing total surface area through increasing microporosity would not be an effective way to improve adsorption for MO. The adsorption characteristics were thought to be further influenced by the structure and morphology of the composites formed, since it was found by SEM that the introduction of silica-coated iron oxides induced the formation of more tightly packed composites with much of their outer surfaces covered in photocatalyst, as opposed to the nonmagnetic counterparts. Additionally, the presence of exposed silica-coated iron oxides on the external surface of the composite after Ag/AgCl deposition was also expected to influence adsorption by changing electrostatic interactions between the dye and A-MAC.

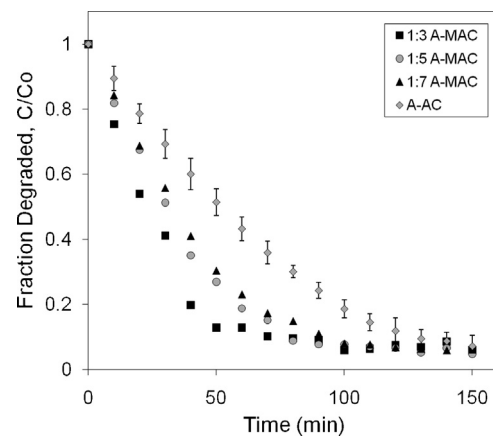


Fig. 10. MO photodegradation by A-MAC composites and A-AC—representative error bars shown.

For example, silica was present in its negatively charged state, since the isoelectric point was previously found to be pH 2 [39], and the surface of Ag/AgCl was thought to also be negatively charged due to termination by Cl⁻ ions and the polarization of the electron distribution in silver relative to AgCl [40]. This may have induced a more negative charge on the A-MAC composites, and changed their interaction with the negatively charged sulfonate groups present in MO, although the MO itself carried an overall amphoteric charge at the slightly acidic pH (~5.5) used in the studies.

Data for the photocatalytic removal was normalized and presented as a temporal course of MO degraded in Fig. 10, where the initial concentration, C_0 (mg L⁻¹), was represented by the equilibrium concentration achieved after 2 h of dark adsorption.

The photocatalytic heterogeneous surface reaction could be described using the Langmuir-Hinshelwood kinetic expression, where the following equation defined reaction rate:

$$\frac{-dC}{dt} = \frac{K k C}{(1 + KC)} \quad (2a)$$

where K is the Langmuir Hinshelwood adsorption coefficient (L mg⁻¹), and k is the reaction rate constant (mg L⁻¹ min⁻¹). This kinetic expression could be simplified into a pseudo-first order equation when the initial concentration used was sufficiently small (<10⁻³ mol L⁻¹ [41]). In this case, $C_0 < 7.7 \times 10^{-5}$ mol L⁻¹, so the pseudo-first order approximation was used. The integrated rate expression is given by:

$$\ln \left(\frac{C_0}{C} \right) = k't \quad (2b)$$

where k' denotes the pseudo-first order rate constant (min⁻¹), which incorporates both the reaction rate constant and the equilibrium adsorption constant. To quantitatively compare photoactivities of the catalysts for the degradation of MO under visible light, the pseudo-first order rate constants were calculated for the initial linear portion of the reaction. Comparison of the fitted and experimental data is shown in Fig. S6, respectively, where the slopes of the fitted lines represented the pseudo-first order rate constants in accordance with Eq. (2b).

From the fitted data, the pseudo-first order rate constants were found to be 0.0298, 0.0213, 0.0191, and 0.0124 min⁻¹ for the 1:3 A-MAC, 1:5 A-MAC, 1:7 A-MAC, and A-AC composites, respectively, with R^2 values between 0.991 and 0.998. The activity of the magnetic composites was greater than that of nonmagnetic A-AC, which may have been due to competitive adsorption of photons by the exposed activated carbon surfaces in the latter material [42], reducing the efficiency of Ag/AgCl excitation. Activity of the magnetic

AC composites was found to increase as the proportion of magnetic component increased, which may have also been caused by reduction of this competitive photon adsorption effect due to suspected changes to composite structure and morphology induced by the introduction of silica-coated iron oxide particles, and more efficient mass transfer between adsorbed methyl orange on the AC and surface active sites of Ag/AgCl. Additionally, as discussed in subsequent sections, positive effects of eluted ionic silver under irradiation may have increased photocatalytic activity for MO degradation by acting as electron traps preventing electron-hole recombination in the magnetic composites. Although the 1:3 A-MAC composite had the highest photocatalytic activity, its saturation magnetization was thought to decline with respect to the 1:5 and 1:7 catalysts, due to the observed phase change of the contained magnetite to a less magnetic or nonmagnetic impurity iron oxide phase. Therefore, the 1:5 A-MAC catalyst was selected for further photoactivity testing as it possessed acceptable magnetization and photoactivity.

3.2.2. Evidence for the photocatalytic degradation of MO

Degradation of MO in photocatalytic systems is reported to occur first by attack on the azo bond by photoproduced reactive species to degrade polyaromatic rings in MO and create mono substituted aromatics. These intermediate molecules may then undergo further radical attack to induce aromatic fragment degradation and eventual mineralization [43]. To probe photocatalytic degradation of MO by the A-MAC composites prepared, changes to the UV-vis absorption spectra of MO were monitored over the course of photodegradation, and results from representative spectra are shown in Fig. S7. The initial spectrum at time $t=0$ (corresponding to the beginning of photocatalysis, after adsorption in the dark) was characterized by a major band around 463 nm due to light absorption by azo bonds in the MO structure, and a smaller peak in the UV range at approximately 265 nm due to absorption by benzene-like structures. With an increase in the photocatalytic treatment time, the spectral height of the azo peak at 463 nm decreased markedly, while the intensity of the band at 265 nm increased. However, past 60 min, this band intensity in the UV range also decreased. These results agreed well with literature, where extended aromatic MO was first degraded by photocatalytic attack to produce benzene-like structures that absorbed in the 200–270 nm range. These intermediates then underwent further degradation as the reaction proceeded [43]. Hydrazine may have also been formed as an intermediate, contributing to the increase in absorbance around 250 nm [44]. The changes in UV-vis spectra evidenced that MO underwent photocatalytic degradation in the irradiated system. It should be noted that the lack of shift in the major band at 463 nm further confirmed that the effect of self-sensitization on MO degradation was negligible [45].

3.2.3. Recyclability

Recyclability of the prepared 1:5 A-MAC composite was studied by performing four consecutive adsorption-photocatalysis cycles, recovering the catalyst between runs by magnetic separation. The photocatalyst performance in these sequential runs is shown in Fig. 11.

The adsorptive capabilities of the composite decreased with sequential runs, and were exhausted after the second cycle. This was thought to be partially due to the inability of the incorporated Ag/AgCl photocatalyst to fully regenerate the adsorptive AC surface during the photocatalysis cycle by degrading all of the adsorbed MO. This also resulted in a decrease in photocatalytic activity with repeated use without regeneration between cycles, since the rate of degradation was lower than the rate of accumulation of MO onto the composite, which saturated the photocatalyst surface and decreased its photonic efficiency [46]. In the second to fourth uses

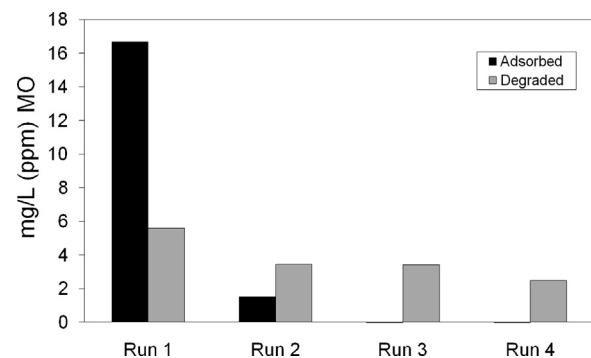


Fig. 11. Adsorption and photodegradation performance of 1:5 A-MAC composite over four consecutive cycles.

of the composite, 70.9%, 63.5%, and 52.6% of the total MO degraded in the first run were decomposed by the recycled material, respectively. This activity was comparable to that previously described for nonmagnetic Ag/AgCl-AC composites, where the amount of MO degraded in the second to fourth runs was 75.2%, 66.8%, and 62.7% of that in the first run, respectively [15]. These reported cycling runs were performed using centrifugation to recover the spent catalyst between trials, where in the current case, magnetic separation was used. The observed decreases in photocatalytic activity of magnetic Ag/AgCl-AC composite compared to its nonmagnetic counterpart may have been due to some catalyst washout that occurred with magnetic separation between runs. Despite this, the similarity in cyclic activities observed indicated that magnetic separation could be employed to recover the spent catalyst. As previously discussed, the decreased efficiency with increased cycle number in the absence of regeneration may have also been attributed to the formation of reaction intermediates and their adsorption and accumulation on the photocatalyst [42,47], as evidenced by Fig. S7. The presence of these intermediates complicated the analysis and interpretation of recyclability of the composite, since the reactive and nonselective photoproduced reactive species were thought to act both on the parent MO compound and on the produced reaction intermediates.

The XRD pattern for the composite catalyst was collected after its cyclic use, and is shown in Fig. 12, with the fresh catalyst pattern for comparison. The patterns before and after cyclic use were very similar, although small peaks at 38.1° and 44.3° were observed in the recycled material due to the (1 1 1) and (2 0 0) faces of metallic

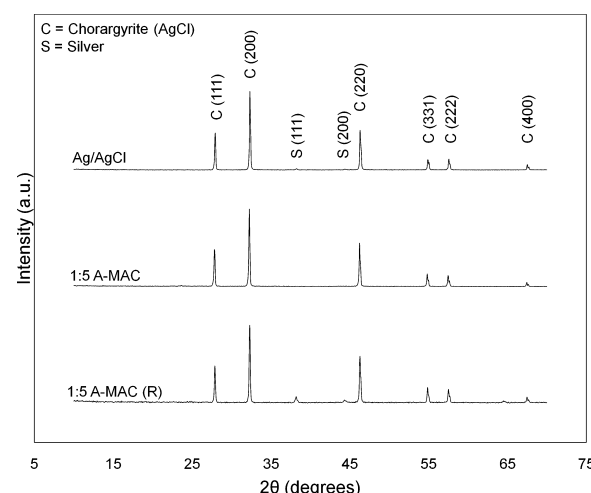


Fig. 12. XRD patterns for as-prepared Ag/AgCl, fresh 1:5 A-MAC composite, and recycled 1:5 A-MAC composite after four adsorption-photocatalysis cycles.

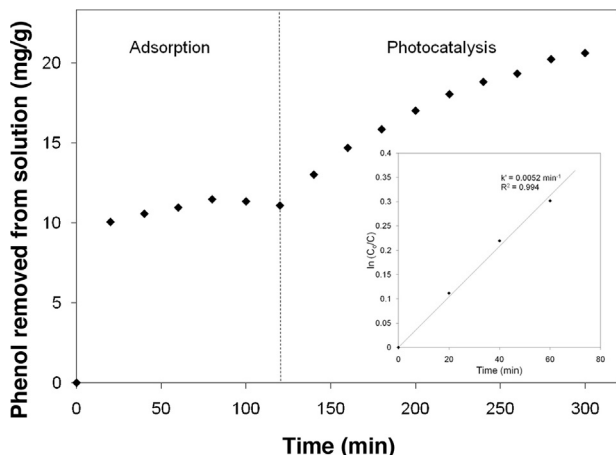


Fig. 13. Adsorption and subsequent photocatalysis using 1:5 A-MAC in 13 mg L⁻¹ phenol solution. Photocatalytic degradation kinetics are shown inset.

silver. The presence of these metallic silver peaks was thought to be due to an increase in the Ag nanoparticle size during visible light photocatalysis, due to aggregation and photoreduction of some AgCl to form additional metallic Ag clusters. This decomposition was reported to have a minor effect on the total surface contents of Ag and AgCl under similar experimental conditions as those used in this study [40,48,49], confirming the stability of such catalysts in repeated use.

3.2.4. Phenol photodegradation

To ensure that the observed activity from Ag/AgCl–magnetic AC composite was due to surface plasmon resonance induced photocatalysis, and was not only caused by photosensitization of organic MO dye under visible light [50], the photodegradation was tested against phenol, a colourless organic target pollutant. The adsorption and subsequent photocatalysis, and associated pseudo-first order kinetics are shown in Fig. 13. The photolytic conversion of phenol was found to be negligible, and the composite exhibited good activity for organics degradation in the absence of a dye-sensitized mechanism, converting about 9.5 mg phenol per gram composite with a pseudo-first order rate constant of 0.0052 min⁻¹. Factors such as adsorption affinity of the pollutant for the composite, initial pollutant concentration, and light penetration in solution were thought to influence the observed differences in photoactivities of A-MAC towards MO and phenol, respectively.

3.2.5. Iron oxide photodissolution

Based on previous reports of photodissolution of iron oxides in photocatalyst/iron oxide systems [8,51,52], the effect of the silica coating was studied for the prepared A-MAC composites. The concentration of iron ions in a 5 g L⁻¹ aqueous catalyst slurry under irradiation was found to be 0.53 ± 0.13 mg L⁻¹ after 60 min and 0.62 ± 0.021 mg L⁻¹ after 150 min, respectively, for the 1:7 A-MAC composite prepared with silica-coated iron oxide particles. These values increased to 1.1 ± 0.042 mg L⁻¹ after 60 min and 1.1 ± 0.033 mg L⁻¹ after 150 min, respectively, for the same composite prepared using uncoated iron oxides. This implied that the silica coating was effective in decreasing the occurrence of iron oxide photodissolution, since the ionic iron concentration in solution was lower for the silica-containing material under irradiation. The photo-Fenton reaction was also thought to be negligible in the photoreactive system due to the low concentrations of Fe obtained. The values of ionic iron were thought to be even lower in the actual photocatalytic systems studied for the degradation of MO and phenol, since a composite dosage of 0.5 g L⁻¹ was used, as opposed to 5 g L⁻¹ used in the control tests.

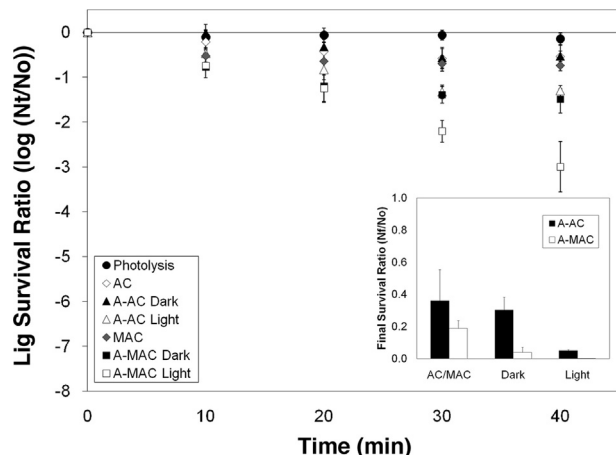


Fig. 14. Inactivation curves for photolysis, AC, A-AC (dark), A-AC (light), 1:5 MAC, 1:5 A-MAC (dark), and 1:5 A-MAC (light), respectively. Catalyst loading was 5 g L⁻¹ (or calculated equivalent for AC/MAC); final survival ratios shown inset.

3.3. Photocatalytic inactivation

Photocatalytic inactivation of a Gram-negative model microorganism, *E. coli* K-12 was studied, as it is a common indicator for faecal contamination [53]. The temporal course of inactivation was quantified for the 1:5 A-MAC composite in dark and light conditions, respectively, and for the 1:5 MAC material itself. The results are shown in Fig. 14, with A-AC for comparison. The photolysis trial performed in the absence of catalyst, indicative of loss of culturability due to damage from the photon source alone, was found to have a negligible effect. Biocompatibility of magnetic AC was tested using an equivalent loading of MAC as that incorporated into the composite, and the final survival ratio was found to be 0.19 ± 0.048, which was comparable to that observed with equivalent neat AC, implying that the incorporation of silica-coated magnetic nanoparticles into the adsorbent did not induce significant toxicity. The population decrease in this case was thought to be due to adsorption of bacteria onto the exposed activated carbon surfaces in MAC. Upon introduction of Ag/AgCl into magnetic AC, an increased loss of cell culturability was observed over that of bacterial adhesion on MAC alone, in both the dark and light conditions using the composite photocatalyst, achieving final survival ratios of 0.04 ± 0.029 and 0.00074 ± 0.001 for each case, respectively.

In the dark, the inactivation was attributed to bacterial adhesion onto the solid catalyst and toxicity of the silver ions eluted. Silver ions are toxic at sub-micromolar concentrations, due to their interaction with enzymes in the respiratory chain reaction, causing the uncoupling of respiration from the synthesis of ATP [54]. Additionally, the Ag⁺ can bind with transport proteins, leading to proton leakage and inducing collapse of proton motive force [55]. These silver ions were formed in the dark by irreversible oxidation of metallic nanosilver and the limited solubility of the AgCl carrier material in saline to form dissolved ionic silver and silver complexes such as AgCl_(aq) or AgCl_x^{1-x}_(aq), that could interact with thiol-containing proteins [56]. The release of silver ions from 5 g L⁻¹ composite into 50 mL distilled deionized water under stirring in the dark was recorded, and the Ag⁺ concentration was found ICP-MS to be 50.8 ± 0.51 mg L⁻¹ after 40 min, and 52.4 ± 0.19 mg L⁻¹ after 60 min, respectively. This was much higher than the 0.53 ± 0.09 mg L⁻¹ previously observed for the A-AC composite after 60 min, and the difference was thought to be due to changes in structure and morphology of the magnetic composite compared to the original A-AC, since the rate of silver ion release was controlled by silver oxidation, which in aqueous

medium depended on the rate of water diffusion and the diffusion characteristics [57]. This diffusion was thought to differ between magnetic and nonmagnetic composites, and the increased silver elution by the A-MAC material caused the increase in dark inactivation capability observed in Fig. 14. It should be noted that the silver ion measurements performed quantified silver ion diffusion into water, which represented an upper limit on the actual diffusion that occurred in saline and in the presence of thiol targets.

This silver ion elution may have also influenced the MO adsorption and degradation observed using the magnetic composites, since the effect of silver ions on photocatalytic degradation of organics is generally reported to increase degradation rate due the electron trapping mechanism of Ag^+ , which reduces recombination of photogenerated charges [58]. For example, in pure photocatalyst systems such as TiO_2 , this enhancement is attributable to the formation of surface adsorbed Ag^+ species, which can become photoreduced and subsequently act as electron traps to prevent recombination [59]. However, the dissolved Ag^+ concentration in the organic degradation studies was expected to be much lower than the value quantified by ICP-MS in the control due to the ten-fold decrease in composite loading used in the photodegradation studies compared to that used for the inactivation studies. In a similar dynamic adsorbent photocatalyst system based on a chitosan- TiO_2 composite [60], doubling the Ag^+ concentration in solution from 100 mg L^{-1} to 200 mg L^{-1} caused a moderate (13.4%) increase in MO photodegradation.

The inactivation capability observed using the magnetic $\text{Ag}/\text{AgCl}-\text{MAC}$ composite increased significantly in the photocatalysis trials, as the production of photoactive species was facilitated by illumination. The results agreed well with the trend observed for nonmagnetic $\text{Ag}/\text{AgCl}-\text{AC}$, where some bactericidal activity was observed in the dark, and inactivation was increased under illumination due to the production of radical and reactive oxygen species [20]. The inactivation realized using the magnetic photocatalyst composite was found to effect a greater loss of culturability to the bacteria than nonmagnetic $\text{Ag}/\text{AgCl}-\text{AC}$, due to its increased silver ion elution, and better photocatalytic efficiency caused by more complete surface coverage of the AC host structure by photocatalyst, reducing competition for photons in the irradiated process. The illumination of the catalyst with visible light was thought to produce electron-hole pairs that could undergo reaction with dissolved oxygen and water to form reactive oxygen species (ROS), which could then interact with the *E. coli* bacteria. The action of ROS on bacteria was found in literature to cause a loss of culturability due to peroxidation of cell wall bilayer functional groups, leading to increased disorder in the bilayer, which increased the fluidity of the cell wall and caused eventual lysis through free efflux of intracellular components [61,62]. The eluted Ag^+ species may have also reduced the rate of recombination of the photoproduced electrons and holes, increasing the photocatalytic efficiency observed. However, it should be noted that, as previously discussed for the $\text{Ag}/\text{AgCl}-\text{AC}$ composite, complications may arise from the use of silver-eluting catalysts in the presence of saline, since binding with free Cl^- may occur past the solubility limit (10^{-5}), causing the formation of AgCl nanoparticles that may then be photoreduced in the irradiated system [63]. Although this may result in the effective regeneration of some Ag/AgCl photocatalyst, its presence is difficult to quantify in the current scheme. Despite this, the approximately 3-log reduction observed in the photocatalytic system indicated that this material possessed good applicability and efficacy for solar photocatalytic disinfection.

3.4. Mechanism of photocatalytic action

The composites were thought to act photocatalytically under visible light through participation of the localized surface plasmon

resonance of the silver nanoparticles formed from partial reduction of AgCl . The generation of holes and electrons occurred in these silver nanoparticles upon the absorption of photons of appropriate wavelengths, and the polarization of charges was induced by the surface plasmon resonance state of the silver. This polarization facilitated effective charge separation of the photogenerated holes and electrons, as the negatively charged electrons were transferred to the silver surface farthest away from the AgCl interface, and the holes transferred to the surface of AgCl [40]. This charge separation was responsible for the stability of silver/silver halide structures, since the generated electrons were prevented from being transferred to Ag^+ in AgCl [64], but were instead transferred to molecular oxygen to form active species such as superoxide [65]. Simultaneously, the holes generated could also oxidize water to produce hydroxyl radicals, or directly oxidize Cl^- ions into Cl^0 , which may have also interacted with target pollutants near the surface of the catalyst [66], and be reduced back to their ionic state. In the adsorbent photocatalyst composites prepared, the role of the activated carbon was to concentrate the pollutant around the photocatalytic active sites, allowing adsorbed pollutant to migrate to the Ag/AgCl decomposition centres present on the adsorbent surface due to concentration gradients [67]. In the absence of adsorbent supports, the pollutant was required to collide with the catalyst and maintain sufficient contact for reaction, after which the intermediates were desorbed back into solution. Additionally, the neat photocatalyst had limited surface area present, which restricted the number of successful collisions with pollutant molecules [68]. In the adsorbent composite, this limitation was overcome, and chain reactions were thought to be promoted since the AC allowed for the retention of reaction intermediates. A schematic of these discussed mechanisms for photocatalytic degradation of organic compounds by the prepared A-MAC composites is given in Fig. S8, and mechanistic pathways for photocatalytic mineralization of MO and phenol investigated in literature were thought to occur to various extents in the irradiated system [69,70].

4. Conclusions and recommendations

In this work, novel magnetic adsorbent photocatalyst composites were synthesized by the preparation of magnetic AC incorporating silica-coated Fe_3O_4 nanoparticles, and a subsequent deposition-precipitation-photoreduction procedure to obtain "egg-shell" structured $\text{Ag}/\text{AgCl}-\text{magnetic AC}$. The resulting composites possessed quasi-superparamagnetic behaviour, and exhibited good visible light induced photocatalytic activity towards the degradation of a model dye, methyl orange, and a colourless organic, phenol. The material could be recovered by an external magnetic field, and possessed some photocatalytic activity in up to four cyclic degradation cycles. The prepared $\text{Ag}/\text{AgCl}-\text{magnetic AC}$ composite also exhibited strong activity for *E. coli* K-12 inactivation, and was able to effect a 3-log reduction in 40 min under irradiation in a 5 g L^{-1} slurry. The visible light induced photodegradation and disinfection capabilities of the composite material, as well as its recovery by magnetic separation, indicate its applicability towards solar detoxification and disinfection schemes using slurry photocatalytic reactors. Future work on this catalyst involves improving its performance in cyclic use, such as through prolonged exposure to irradiation to regenerate the activated carbon surface [71]. Additionally, the role of dissolved silver in photocatalytic organics degradation and microbial inactivation should be clarified in both dark and light conditions for the prepared composites. Optimization of the adsorptive, photocatalytic, and magnetic behaviours of the developed composites should also be undertaken. One strategy proposed to improve the magnetic removal efficiency is by improving the photocatalyst activity to reduce the equivalent composite weight, such as through

morphology-controlled synthesis of high-performance Ag/AgCl [72]. The effect of operational parameters such as light intensity, solution concentration, and pH on the resulting photoactivity of the prepared composites should also be studied in the future.

Acknowledgements

This work was supported by the Natural Sciences and Engineering Research Council of Canada. The authors would like to acknowledge Dr. Alexander Mommers and Dr. Yong Yang at the Centre for Catalysis Research and Innovation (University of Ottawa), Dr. Jianqun Wang (Carleton University), and Dr. Paul Dubé from the Brockhouse Institute for Materials Research (McMaster University) for their help with characterizations. Dr. Nimal De Silva from the University of Ottawa is also thanked for help with ICP-MS analysis.

Appendix A. Supplementary data

Supplementary data associated with this article can be found, in the online version, at <http://dx.doi.org/10.1016/j.apcatb.2014.04.043>.

References

- [1] N. Serpone, J. Phys. Chem. B 110 (2006) 24287–24293.
- [2] P. Wang, B. Huang, X. Zhang, X. Qin, H. Jin, Y. Dai, Z. Wang, J. Wei, J. Zhan, S. Wang, J. Wang, M.-H. Whangbo, Chem. Eur. J. 15 (2009) 1821–1824.
- [3] A. Pourahmad, S. Sohrabnezhad, E. Kashefian, Spectrochim. Acta, A: Mol. Biomol. Spectrosc. 77 (2010) 1108–1114.
- [4] J. Matos, J. Laine, J.M. Herrmann, Appl. Catal., B: Environ. 18 (1998) 281–291.
- [5] H. Slimen, A. Houas, J.P. Nogier, J. Photochem. Photobiol., A: Chem. 221 (2011) 13–21.
- [6] X. Wang, Y. Liu, Z. Hu, Y. Chen, W. Liu, G. Zhao, J. Hazard. Mater. 169 (2009) 1061–1067.
- [7] T.-T. Lim, P.-S. Yap, M. Srinivasan, A.G. Fane, Crit. Rev. Env. Sci. Technol. 41 (2011) 1173–1230.
- [8] D. Beydoun, R. Amal, G.K.C. Low, S. McEvoy, J. Phys. Chem. B 104 (18) (2000) 4387–4396.
- [9] R. Buonsanti, V. Grillo, R. Carlino, C. Giannini, M.L. Curri, C. Innocenti, C. Sangregorio, K. Achterhold, F.G. Parak, A. Agostiano, P.D. Cozzoli, J. Am. Chem. Soc. 128 (51) (2006) 16953–16970.
- [10] M. Ye, Q. Zhang, X. Hu, J. Ge, Z. Lu, L. He, Z. Chen, Y. Yin, Chem. Eur. J. 16 (21) (2010) 6243–6250.
- [11] C. An, X. Ming, J. Wang, S. Wang, J. Mater. Chem. 22 (11) (2012) 5171–5176.
- [12] Y. Ao, J. Xu, D. Fu, C. Yuan, Carbon 46 (4) (2008) 596–603.
- [13] Y. Ao, J. Xu, D. Fu, X. Shen, C. Yuan, Sep. Purif. Technol. 61 (3) (2008) 436–441.
- [14] Y. Ao, J. Xu, D. Fu, C. Yuan, J. Alloys Compd. 471 (1–2) (2009) 33–38.
- [15] J. Gamage McEvoy, W. Cui, Z. Zhang, Appl. Catal., B: Environ. 144 (2014) 702–712.
- [16] X. Wang, X. Tang, Z. Chen, T.-T. Lim, J. Mater. Chem. 22 (2012) 23149–23158.
- [17] S.-J. Park, Y.-S. Jang, J. Colloid Interface Sci. 261 (2003) 238–243.
- [18] Y.L. Wang, Y.Z. Wan, X.H. Dong, G.X. Cheng, H.M. Tao, T.Y. Wen, Carbon 36 (11) (1998) 1567–1571.
- [19] H. Le Pape, F. Solano-Serena, P. Contini, C. Devillers, A. Maftah, P. Leprat, J. Inorg. Biochem. 98 (2004) 1054–1060.
- [20] J. Gamage McEvoy, D.A. Bilodeau, W. Cui, Z. Zhang, J. Photochem. Photobiol., A: Chem. 267 (2013) 25–34.
- [21] J.H. Meng, G.Q. Yang, L.M. Yan, X.Y. Wang, Dyes Pigm. 66 (2005) 109–113.
- [22] G. Li, K.H. Wong, X. Zhang, C. Hu, J.C. Yu, R.C.Y. Chan, P.K. Wong, Chemosphere 76 (2009) 1185–1191.
- [23] W. Stöber, A. Fink, E. Bohn, J. Colloid Interface Sci. 26 (1968) 62–69.
- [24] W. Li, C. Liang, W. Zhou, J. Qiu, Z. Zhou, G. Sun, Q. Xin, J. Phys. Chem. B 107 (2003) 6292–6299.
- [25] R.J. Gilkes, A. Sudhiprakarn, J. Soil Sci. 30 (1979) 357–361.
- [26] T.W. Swaddle, P. Oltmann, Can. J. Chem. 58 (1980) 1763–1772.
- [27] Y.T. He, S.J. Traina, Clay Miner. 42 (2007) 13–19.
- [28] C. Hu, T. Peng, X. Hu, Y. Nie, X. Zhou, J. Qu, H. He, J. Am. Chem. Soc. 132 (2010) 857–862.
- [29] J.-F. Guo, B. Ma, A. Yin, K. Fan, W.-L. Dai, Appl. Catal., B: Environ. 101 (2011) 580–586.
- [30] K.S.W. Sing, D.H. Everett, R.A.W. Haul, L. Moscou, R.A. Pierotti, J. Rouquérol, T. Siemieniewska, Pure Appl. Chem. 57 (1985) 603–619.
- [31] J. Rouquérol, D. Avnir, C.W. Fairbridge, D.H. Everett, J.H. Haynes, N. Pernicone, J.D.F. Ramsay, K.S.W. Sing, K.K. Unger, Pure Appl. Chem. 66 (1994) 1739–1758.
- [32] X. Zhang, L. Lei, J. Hazard. Mater. 153 (2008) 827–833.
- [33] X. Glauz, G. Calzaferri, Photochem. Photobiol. Sci. 2 (2003) 398–401.
- [34] B.R.S. Lemos, A.P.C. Teixeira, J.D. Ardisson, W.A.A. Macedo, L.E. Fernandez-Outon, C.C. Amorim, F.C.C. Moura, R.M. Lago, Appl. Sci. 2 (2012) 513–524.
- [35] M. Villani, T. Rimoldi, D. Calestani, L. Lazzarini, V. Chiesi, F. Casoli, F. Albertini, A. Zappettini, Nanotechnology 24 (2013), Article ID# 135601 (9 pages).
- [36] Z. He, T. Hong, J. Chen, S. Song, Sep. Purif. Technol. 96 (2012) 50–57.
- [37] X. Zhuang, Y. Wang, C. Feng, Y. Shen, D. Zhao, Chem. Mater. 21 (2009) 706–716.
- [38] C. Pelekani, V.L. Snoeyink, Water Res. 33 (1999) 1209–1219.
- [39] M. Luo, D. Bowden, P. Brimblecombe, Water Air Soil Pollut. 198 (2009) 233–241.
- [40] P. Wang, B. Huang, X. Qin, X. Zhang, Y. Dai, J. Wei, M.-H. Whangbo, Angew. Chem. Int. Ed. 47 (2008) 7931–7933.
- [41] J.-M. Herrmann, Catal. Today 53 (1999) 115–129.
- [42] Y.H. Ao, J.J. Xu, D.G. Fu, X.W. Shen, C.W. Yuan, Colloids Surf., A: Physicochem. Eng. Aspects 312 (2008) 125–130.
- [43] S. Al-Qaradawi, S.R. Salman, J. Photochem. Photobiol., A: Chem. 148 (2002) 161–168.
- [44] L.-C. Chen, F.-R. Tsai, C.-M. Huang, J. Photochem. Photobiol., A: Chem. 170 (2005) 7–14.
- [45] Y. Zang, R. Farnood, Appl. Catal., B: Environ. 79 (2008) 334–340.
- [46] J. Araña, J.L. Martínez Nieto, J.A. Herrera Melián, J.M. Doña Rodríguez, O. Gondález Díaz, J. Pérez Peñam, O. Bergasa, C. Alvarez, J. Méndez, Chemosphere 55 (2004) 893–904.
- [47] S.X. Liu, X.Y. Chen, X. Chen, J. Hazard. Mater. 143 (2007) 257–263.
- [48] P. Wang, B. Huang, Z. Lou, X. Zhang, X. Qin, Y. Dai, Z. Zheng, X. Wang, Chem. Eur. J. 16 (2010) 538–544.
- [49] D. Wang, Y. Duan, Q. Luo, X. Li, J. An, L. Bao, L. Shi, J. Mater. Chem. 22 (2012) 4847–4854.
- [50] T. Wu, G. Liu, J. Zhao, H. Hidaka, N. Serpone, J. Phys. Chem. B 102 (30) (1998) 5845–5851.
- [51] J. Navio, G. Colon, M. Trillas, J. Peral, X. Domenech, J.J. Testa, J. Padron, D. Rodriguez, M.I. Litter, Appl. Catal., B: Environ. 16 (1998) 187–196.
- [52] M.I. Litter, J.A. Navio, J. Photochem. Photobiol., A: Chem. 84 (1994) 183–193.
- [53] J. Marugán, R. van Grieken, C. Pablos, C. Sordo, Water Res. 44 (3) (2010) 789–796.
- [54] K. Holt, A. Bard, Biochemistry 44 (2005) 13214–13223.
- [55] C. Lok, C. Ho, R. Chen, Q. He, W. Yu, H. Sun, P. Tam, J. Chiu, C. Che, J. Proteome Res. 5 (2006) 916–924.
- [56] S. Liau, D. Read, W. Pugh, J. Furr, A. Russell, Lett. Appl. Microbiol. 25 (1997) 279–283.
- [57] R. Kumar, H. Münsch, Biomaterials 26 (2005) 2081–2088.
- [58] M.I. Litter, Appl. Catal., B: Environ. 23 (1999) 89–114.
- [59] A. Dobosz, A. Sobczyński, Water Res. 37 (2003) 1489–1496.
- [60] X. Zhao, Q. Li, X. Zhang, H. Su, K. Lan, A. Chen, Environ. Prog. Sustainable Energy 30 (4) (2011) 567–575.
- [61] C. Puigarin, J. Kiwi, V. Nadtochenko, Appl. Catal., B: Environ. 128 (2012) 179–183.
- [62] T. Saito, T. Iwase, J. Horie, T. Morioka, J. Photochem. Photobiol., B: Biol. 14 (1992) 369–379.
- [63] J. Liu, D.A. Sonshine, S. Shervani, R.H. Hurt, ACS Nano 4 (11) (2010) 6903–6913.
- [64] H. Xu, H. Li, J. Xia, S. Yin, Z. Luo, L. Liu, L. Xu, ACS Appl. Mater. Interfaces 3 (2011) 22–29.
- [65] J. Yu, G. Dai, B. Huang, J. Phys. Chem. C 113 (2009) 16394–16401.
- [66] D. Wang, Y. Duan, Q. Luo, X. Li, L. Bao, Desalination 270 (2011) 174–180.
- [67] W. Li, S. Liu, Adsorption 18 (2012) 67–74.
- [68] R. Leary, A. Westwood, Carbon 49 (2011) 741–772.
- [69] C. Baiocchi, M.C. Brusino, E. Pramauro, A.B. Prevot, L. Palmisano, G. Marci, Int. J. Mass Spectrom. 214 (2002) 247–256.
- [70] E. Grabowska, J. Reszczynska, A. Zaleska, Water Res. 46 (2012) 5453–5471.
- [71] P.-S. Yap, T.-T. Lim, Water Res. 46 (2012) 3054–3064.
- [72] M. Zhu, P. Chen, M. Liu, J. Mater. Chem. 21 (2011) 16413–16419.